

Encoding a magic state with beyond break-even fidelity

Riddhi S. Gupta,^{1,2} Neereja Sundaresan,¹ Thomas Alexander,¹ Christopher J. Wood,¹ Seth T. Merkel,¹ Michael B. Healy,¹ Marius Hillenbrand,³ Tomas Jochym-O'Connor,^{1,2} James R. Wootton,⁴ Theodore J. Yoder,¹ Andrew W. Cross,¹ Maika Takita,¹ and Benjamin J. Brown^{1,5}

¹*IBM Quantum, T. J. Watson Research Center, Yorktown Heights, New York 10598, USA*

²*IBM Quantum, Almaden Research Center, San Jose, California 95120, USA*

³*IBM Deutschland Research & Development GmbH, Boeblingen, Germany*

⁴*IBM Quantum, IBM Research Zurich, Switzerland*

⁵*IBM Denmark, 2605 Brøndby, Denmark*

We distill magic states to complete a universal set of fault-tolerant logic gates that is needed for large-scale quantum computing. By encoding better quality input states for our distillation procedure, we can reduce the considerable resource cost of producing magic states. We demonstrate an error-suppressed encoding scheme for a two-qubit input magic state, that we call the CZ state, on an array of superconducting qubits. Using a complete set of projective logical Pauli measurements, that are also tolerant to a single circuit error, we propose a circuit that demonstrates a magic state prepared with infidelity $(1.87 \pm 0.16) \times 10^{-2}$. Additionally, the yield of our scheme increases with the use of adaptive circuit elements that are conditioned in real time on mid-circuit measurement outcomes. We find our results are consistent with variations of the experiment, including where we use only post-selection in place of adaptive circuits, and where we interrogate our output state using quantum state tomography on the data qubits of the code. Remarkably, the error-suppressed preparation experiment demonstrates a fidelity exceeding that of the preparation of the same unencoded magic-state on any single pair of physical qubits on the same device.

Introduction. Large-scale quantum algorithms demand that we can produce a quantum computer that performs a universal set of high-fidelity logic gates using noisy devices. To this end we look for fault-tolerant ways of processing encoded quantum information such that we can detect and account for errors using auxiliary qubits [1–6]. Given a large supply of high-fidelity magic states we can perform a universal set of logic gates with low-density parity-check code architectures by gate teleportation [7–12]. High-fidelity magic states are produced [13–15] by processing noisy input magic states with fault-tolerant distillation circuits, where experimental progress to prepare input magic states using trapped-ion architectures is described in Refs. [4, 5]. It is expected that a considerable amount of the resources of a quantum computer will be occupied performing magic state distillation schemes and, as such, it is valuable to find ways of reducing its cost. One way to reduce its resource cost is to improve the fidelity of input states [15–21], such that magic states can be distilled with less resource-intensive circuits.

Here we propose and implement an error-suppressed encoding circuit to prepare a state that is input to magic-state distillation using a heavy-hexagonal lattice of superconducting qubits [2, 3, 22]. Our circuit prepares an input magic state, that we call a CZ state, encoded on a four-qubit error-detecting code. CZ states can be used to prepare Toffoli states [23] that can be distilled [15] for use in important quantum algorithms. Our circuit is capable of detecting any single error during state preparation, as such, the infidelity of the encoded state is suppressed as $\mathcal{O}(\epsilon^2)$ where ϵ is the probability that a circuit element experiences an error. In contrast a standard encoding circuit prepares an input state with infidelity $\mathcal{O}(\epsilon)$. Furthermore, we can improve the yield of the magic states

we successfully prepare with the error-suppressed circuit using adaptive circuits that are conditioned in real time on the outcomes of mid-circuit measurements. We propose several tomographical experiments to interrogate the preparation of the magic state, including a complete set of fault-tolerant projective logical Pauli measurements, that can also tolerate the occurrence of a single error during readout.

Magic state preparation and logical tomography.
We prepare the CZ-state:

$$|CZ\rangle = \frac{|00\rangle + |01\rangle + |10\rangle}{\sqrt{3}},$$

encoded on a distance-2 error-detecting code where distinct bit-strings label orthogonal computational basis states over two qubits. We can achieve the CZ-state by, first, preparing the $|+\rangle = \sum_{a,b=0,1} |ab\rangle/2$ state and, then, projecting it onto the $CZ = +1$ eigenspace of the controlled-phase (CZ) operator $CZ = \text{diag}(1, 1, 1, -1)$, i.e. $|CZ\rangle \propto \Pi^+|+\rangle$ with the projector $\Pi^+ = (\mathbb{1} + CZ)/2$. We can perform both of these operations with the four-qubit code. Specifically, it has a fault-tolerant preparation of the $|+\rangle$ state and, as we will show, we can make a fault-tolerant measurement of the logical CZ operator to prepare an encoded CZ-state.

Encoded states of the four-qubit code lie in the common $+1$ eigenvalue eigenspace of its stabilizers $S^X = X \otimes X \otimes X \otimes X$, $S^Z = Z \otimes Z \otimes Z \otimes Z$, and $S^Y = S^Z S^X$ where X and Z are the standard Pauli matrices. The four-qubit code encodes two logical qubits that are readily prepared in a logical $|\mp\mp\rangle$ state by initializing four data qubits in the superposition state, $|+\rangle \propto |0\rangle + |1\rangle$, and measuring S^Z . We note that we use bars to indicate we are describing states and operations in the logical sub-

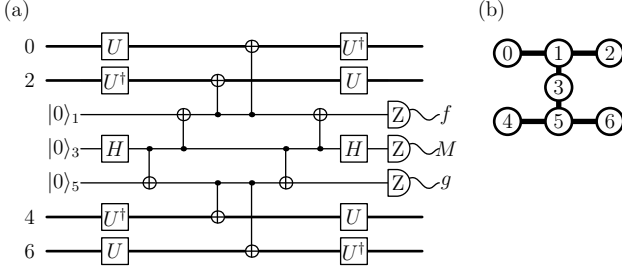


FIG. 1: A fault-tolerant circuit (a) to measure S^X , S^Z and \bar{W} using flag qubits on the heavy-hexagonal lattice architecture (b). The four-qubit code is encoded on qubits with even indices and the other qubits are used to make the fault-tolerant parity measurement. The circuit measures S^X (S^Z) by setting $U = \mathbb{1}$ (H), where H is the Hadamard gate. As explained in the main text, the circuit measures \bar{W} if we set $U = T$. Measurement outcome M gives the reading of the parity measurement, and outcomes f and g flag that the circuit may have introduced a logical error to the data qubits.

space. We prepare the state with $S^Z = +1$, using either post selection or, alternatively, an adaptive Pauli-X rotation on a single qubit given a random -1 outcome from the S^Z measurement.

The four-qubit code has a transversal implementation of the CZ-gate on its encoded subspace, $\bar{CZ} \simeq \sqrt{Z} \otimes \sqrt{Z}^\dagger \otimes \sqrt{Z}^\dagger \otimes \sqrt{Z}$, where $\sqrt{Z} = \text{diag}(1, i)$. We can measure this operator as follows. We note that conjugating S^X with the unitary rotation $\tilde{T} = T \otimes T^\dagger \otimes T^\dagger \otimes T$, where $T = \text{diag}(1, \sqrt{i})$, gives the hermitian operator:

$$\bar{W} \equiv \tilde{T} S^X \tilde{T}^\dagger \propto \bar{CZ} S^X. \quad (1)$$

Given that we prepare the code with $S^X = +1$, measuring \bar{W} effectively gives a reading of \bar{CZ} .

It is essential to our scheme that we reach the $S^Z = +1$ eigenspace. This is due to the non-trivial commutation relations of \bar{W} with the stabilizers of the code [24, 25]. We have the group commutation relation, $\bar{W} S^X \bar{W}^{-1} S^X^{-1} = S^Z$, revealing that \bar{W} only commutes with S^X in the $S^Z = +1$ subspace. If $S^Z = -1$, the group commutator reveals that \bar{W} and S^X anti-commute, and are therefore incompatible observables in this subspace.

We can perform all of the aforementioned measurements, S^X , \bar{W} and S^Z , on the heavy-hexagon lattice geometry [22]. We show one such setup in Fig. 1. Essential to the fault-tolerant procedure are flag fault-tolerant readout circuits [2, 3, 22, 26], that identify errors that occur during the parity measurement.

We therefore present a sequence of measurements that prepare the input magic state and, in tandem, identifies a single error that may have occurred during the preparation procedure. We show the sequence in Fig. 2 and describe its function in the figure caption. As we can detect a single error, we expect the infidelity of the output state to be $\mathcal{O}(\epsilon^2)$ where ϵ is the error rate of a single operation of the preparation circuit.

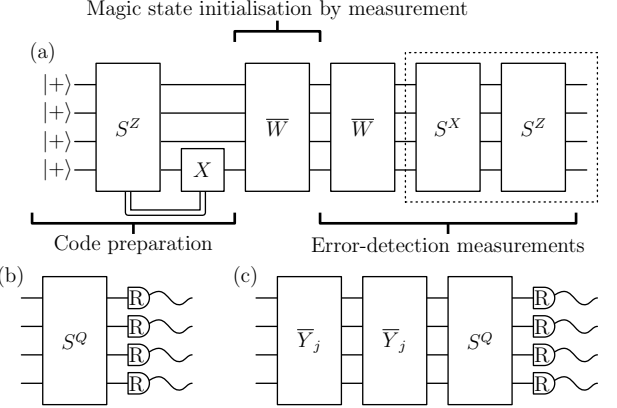


FIG. 2: (a) The preparation of a CZ-state on a four-qubit code in three steps. In the code preparation step, the four-qubit code is prepared in the logical $|++\rangle$ state by measuring $|+\rangle^{\otimes 4}$ with the S^Z operator. We can use adaptive circuits or post-selection to correct for $S^Z = -1$ outcomes. In the magic state initialization step we measure the \bar{W} operator and post-select on the $+1$ outcome. In the final error-detection step we identify errors that may have occurred during preparation. We measure \bar{W} a second time to identify if a measurement error occurred during the magic state initialization step. We finally measure S^X and S^Z a second time to identify Pauli errors that may have occurred or if the initial S^Z measurement gave a readout error. We replace the parity measurements in the dashed box of (a) with circuits (b) and (c) to make logical tomographic measurements and, at the same time, infer a complete set of stabilizer data for error detection. For example, if we set $S^Q = S^X$ and measure qubits in the $R = Z$ basis, we infer the value of S^Z , as in (a), and we also obtain readings of the logical \bar{Z}_1 , \bar{Z}_2 and $\bar{Z}_1 \bar{Z}_2$. Likewise, we can set $S^Q = S^Z$ and $R = X(Y)$ to infer S^X (S^Y) as well as logical Pauli operators \bar{X}_1 , \bar{X}_2 and $\bar{X}_1 \bar{X}_2$ ($\bar{X}_1 \bar{Z}_2$, $\bar{Z}_1 \bar{X}_2$ and $\bar{Y}_1 \bar{Y}_2$). In (c) we include a \bar{Y}_j measurement for logical qubit $j = 1, 2$ to measure logical operators of the form \bar{Y}_j , $\bar{Y}_j \bar{X}_k$ and $\bar{Y}_j \bar{Z}_k$ with $k \neq j$ and $k = 1, 2$, and an appropriate choice of R . The \bar{Y}_j operator is measured twice to identify the occurrence of measurement errors. Operators \bar{Y}_j are supported on three of the data qubits and can therefore be read out with an appropriate modification to the circuit shown in Fig. 1.

We compare our error-suppressed magic-state preparation scheme to a standard scheme for encoding a two-qubit magic state, as well as a circuit that prepares the magic state on two physical qubits. Both of these schemes are described in Appendix A.

We verify our state preparation schemes by performing two variants of quantum state tomography to reconstruct the logical state. The first method uses fault-tolerant circuits that directly measure the logical operators, we refer to this novel tomographical method as ‘logical tomography’. For the second method, which we refer to as ‘physical tomography’, we perform standard state tomography on the full state of the four data qubits of the system and then project the reconstructed state into the logical subspace. Logical tomography with the four-qubit code is summarized in Fig. 2(b)-(c). All of our logical tomog-

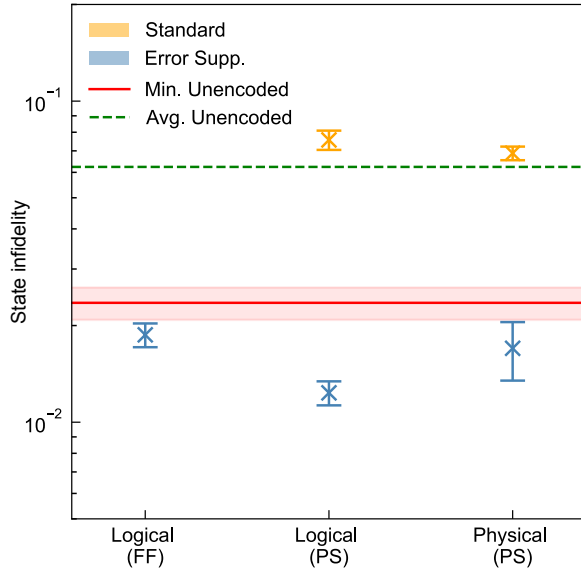


FIG. 3: State infidelity for the error-suppressed (blue) vs. standard (orange) schemes. On the x -axis, a state is reconstructed with either logical or physical tomography. The correction for the initial S^Z measurement in Fig. 2(a) is implemented either using real-time feedforward (FF) or post-selection (PS). For the Physical data points, the state from physical tomography is projected onto the logical subspace before computing infidelity by fitting to ideal projectors. Error-bars represent 1σ from bootstrapping. For all tomographic methods, the error-suppressed scheme achieves a lower state infidelity compared to the standard scheme. The unencoded magic state prepared directly on two physical qubits gives an average infidelity across 28 qubit pairs as $\approx 6.2 \times 10^{-2}$ (green dashed) using 18 repetitions over a 24-hour period with 10^5 shots/circuit. Of these, the best performing pair yields a minimum infidelity of $(2.354 \pm 0.271) \times 10^{-2}$ (red solid). In all cases, the error-suppressed scheme outperforms the best two-qubit unencoded magic state.

raphy circuits can tolerate a single error at the readout stage, by repeating the measurement of logical operators, and by comparing measurement outcomes to earlier readings of stabilizers.

Logical tomography is more efficient than physical tomography since we are directly measuring and reconstructing the encoded logical state, rather than the physical state. In the case of the four-qubit code this requires only 7 distinct circuits, whereas physical tomography requires us to sample 81 different measurement circuits.

Experimental results. We performed our experiments using IBM Quantum’s first-generation real-time control system architecture deployed on `ibm_peekskill`; one of the IBM Quantum Falcon Processors [27]. Device characterization can be found in Appendix B. The control system architectures gives us access to dynamic circuit operations, such as real-time adaptive circuit operations that depend on the outcomes of mid-circuit measurements,

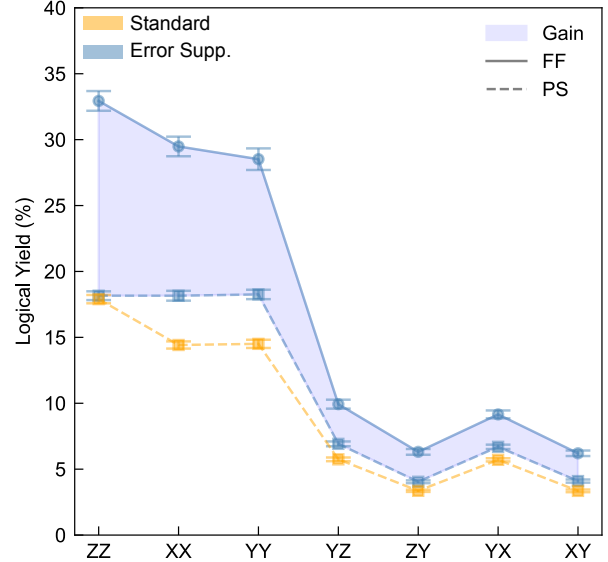


FIG. 4: Yield or acceptance rate after post-selection (%) vs. Logical tomography circuits from Fig. 2 (b),(c) for the error-suppressed scheme with feedforward (blue circles) vs. post-selection (blue squares); standard scheme shown for reference (orange squares). Error-bars represent 1σ from bootstrapping. Yield for the error-suppressed scheme (shaded region) increases from $18.16 \pm 0.05\%$ to $30.3 \pm 1.9\%$ ($5.4 \pm 1.4\%$ to $7.9 \pm 1.7\%$) for circuits in Fig. 2 (b) (Fig. 2 (c)) where the standard deviation represents variation over logical Pauli directions. The yield for standard scheme is $15.6 \pm 1.6\%$ ($4.5 \pm 1.2\%$) for Fig. 2 (b) (Fig. 2 (c)). For reference, the acceptance rate after post-selection for physical tomography experiments (not shown) is measured to be $14.9 \pm 0.1\%$ ($20.9 \pm 0.1\%$) for the error-suppressed (standard) scheme, where the standard deviation represents variation over 81 physical Pauli directions.

i.e., feedforward [28], see Appendix C for details.

Our results are summarized in Fig. 3 where we present state infidelities for various state preparation schemes calculated using both logical and physical tomography. For results described in the main text we model the reconstructed state assuming readout is conducted with projective measurements. We also present an alternative analysis in Appendix D where we combine readout error characterization with tomographic reconstruction using noisy positive operator-valued measurements.

To accommodate drift in device parameters over the data collection period, a complete set of tomography circuits were interleaved and submitted in batches of $\sim 10^4$ shots until a total of $\sim 10^6$ shots were collected over several days. The resulting counts database is uniformly sampled with replacement for ten bootstrap trials with batch size limited to 20% of the total database before post-selection. The standard deviation, σ , of these bootstrapped trials are plotted as error bars in all data figures.

All tomographic fitting was done using positive-semidefinite constrained weight-least-squares convex op-

timization using the Qiskit Experiments tomography module [29]. For logical tomography the fitting weights were set proportional to inverse of the standard errors for each logical Pauli expectation value estimate. These weights accommodate the different logical yield rates for each logical Pauli measurement. The logical yield for each basis measurement is shown in Fig. 4 and discussed in more detail below.

We first compare the state preparation scheme using dynamic circuits against the same preparation scheme executed with static circuits and post-selection. This comparison is conducted using logical tomography. These are the left and middle data points displayed in blue in Fig. 3, respectively. We find that the infidelities are commensurate for these two experiments. Using dynamic circuits with feedforward operations, we encode a two-qubit error-suppressed input magic-state with a logical infidelity $(1.87 \pm 0.16) \times 10^{-2}$. In the post-selection experiment, we obtain an infidelity of $(1.23 \pm 0.11) \times 10^{-2}$. The feedforward operations in our experiment can introduce idling periods, of the order of hundreds of nanoseconds, during which time additional errors can accumulate. We attribute this idling time to the difference in fidelity between these preparation schemes.

We find that the use of dynamic circuits significantly increases the yield of magic states, see Fig. 4. For logical tomography, the acceptance rate after post-selection varies by the choice of measurement bases. The logical-tomography circuits of the form shown in Fig. 2(b) yield show the largest increase in yield, from $\approx 18\%$ to $\approx 30\%$. The remaining tomography circuits, of the form of Fig. 2(c), have a yield increased from $\approx 5\%$ to $\approx 8\%$. As we have already discussed, the improvement in the rate at which input CZ states are produced is obtained without a substantial loss of state fidelity.

We can analyze the commonly occurring errors for fault-tolerant circuits using syndrome outcomes to infer the events that are likely to have caused them [30]. This is done using the method detailed in Appendix E for the results of the error-suppressed scheme, without any post-selection. Assuming an uncorrelated error model, we find that the average probability per single error event is 0.19% with a standard deviation of 0.11%. The highest value is 1.2%, corresponding to errors during the final stabilizer measurement which spread to and are detected by the flag qubits. Similar errors for the other measurement rounds show the probability rising from 0.35% for the first to 0.41% and 0.45% for the following two. This could suggest that, rather than being caused by Pauli errors, other effects such as an accumulation of leakage on the flag qubits may be the cause of these results.

We verify the performance of our logical tomography procedure by comparing our results to the infidelity obtained using physical tomography for the magic state preparation procedure scheme where we obtain the $S^Z = +1$ eigenspace with post-selection. The fitter weights in this case are the standard Gaussian weights based on the observed frequencies of each projective measurement

outcome of each basis element. In physical tomography, the yield after post-selection is constant in all 81 measurement bases. To compare the infidelity obtained with physical tomography evenhandedly with that obtained using logical tomography, we reconstruct the logical subspace from the density matrix obtained from physical tomography on the data qubits of the code, ρ_{phys} . The logical subspace is obtained by projecting ρ_{phys} onto the logical subspace, see, e.g., Ref. [31, 32]. We obtain the elements of the density matrix of the logical subspace ρ via the equation:

$$\rho_{kl,mn} = \frac{\langle \bar{k} \bar{l} | \rho_{\text{phys}} | \bar{m} \bar{n} \rangle}{P_L}, \quad (2)$$

where $k, l, m, n = 0, 1$ specify orthogonal vectors in the logical subspace and $P_L = \sum_{k,l} \langle \bar{k} \bar{l} | \rho | \bar{k} \bar{l} \rangle$ is the probability that the state is prepared is in the logical subspace. Using this method we obtain projected logical infidelity $(1.70 \pm 0.35) \times 10^{-2}$ with the probability of finding ρ_{phys} in the logical subspace $P_L = 0.898 \pm 0.008$. An average post-selection acceptance rate over all physical Pauli directions is found to be $14.9 \pm 0.1\%$. This data point is shown in blue to the right of Fig. 3 to be compared with the central blue data point. This demonstrates consistency between logical and physical tomography. For reference, raw state fidelities from physical tomography prior to logical projection are reported in Appendix D.

We compare our error-suppressed magic state preparation procedure to a standard static circuit that encodes a physical copy of the magic state into the four-qubit code. In this standard scheme, we obtain an infidelity of $(7.56 \pm 0.52) \times 10^{-2}$ using logical tomography and $(6.88 \pm 0.33) \times 10^{-2}$ using physical tomography with logical projection. In the case of physical tomography, the encoded state on the four data qubits has a post-selection acceptance rate of $20.9 \pm 0.1\%$, and the reconstructed density matrix is found in the code space with probability $P_L = 0.789 \pm 0.004$. We show these data points in Fig. 3 with orange markers. Our experiments consistently demonstrate that our error-suppressed encoding scheme has an infidelity at least $4 \times$ smaller than a standard scheme to encode magic states.

Finally, we compare our error-suppressed preparation procedure to a state preparation experiment performed using physical qubits. We mark the lowest infidelity we obtained over all of the adjacent pairs of physical qubits on the 27 qubit device, $(2.4 \pm 0.3) \times 10^{-2}$, with a red line in Fig. 3. Remarkably, all fidelities for all of our error-suppressed magic-state preparation schemes exceed the fidelity of a simple experiment to prepare the CZ state with physical qubits.

Discussion. To summarize, we have presented a scheme that encodes an input magic state with a fidelity higher than we can achieve with any pair of physical qubits on the same device using basic entangling operations. This improvement in fidelity, that takes us beyond the break even point set by basic physical qubit operations, can be attributed to quantum error correction which suppresses

noise that accumulates during our preparation circuit.

We have shown that experimental progress has reached a point where we can engineer and develop small gadgets that will impact on the resource cost of large-scale quantum computers. In our case, we have benefited additionally from the use of dynamic circuits where mid-circuit measurements condition gates operations in real time to improve the efficacy of magic state distillation protocols. In the future it will be exciting to continue to design, develop and test new gadgets with real hardware, that will improve the performance of the key subroutines needed for fault-tolerant quantum computing.

Acknowledgements. We acknowledge the use of IBM Quantum services for this work. These system capabilities are available as open-access to device users. We also acknowledge the work of the IBM Quantum software and hardware teams that enabled this project. The views expressed are those of the authors, and do not reflect the official policy or position of IBM or the IBM Quantum team. B.J.B. is grateful for the hospitality of the Center for Quantum Devices at the University of Copenhagen. J.R.W. acknowledges support from the NCCR SPIN, a National Centre of Competence in Research, funded by the Swiss National Science Foundation (grant number 51NF40-180604). R.S.G. and S.T.M. acknowledge support from the Army Research Office under QCISS (W911NF-21-1-0002). T.A., M.H., and M.B.H. acknowledge support from IARPA under LogiQ (contract W911NF-16-1-0114) on real-time control software work. All statements of fact, opinion or conclusions contained herein are those of the authors and should not be construed as representing the official views or policies of the US Government.

Author contributions. R.S.G., N.S., T.A., M.H., M.B.H. enabled experimental execution using real-time control flow; S.T.M. performed unencoded magic-state tomography experiments, R.S.G. performed encoded magic-state tomography experiments and simulations; C.J.W., S.T.M. conceived and developed tomographic fitting procedures, with and without error-mitigation, implemented by R.S.G.; R.S.G., C.J.W., S.T.M., J.R.W., M.T. and B.J.B. performed data analysis; T.J., T.Y., A.W.C. and B.J.B. developed the fault-tolerant magic-state preparation circuits that were initially conceived of by B.J.B.; R.S.G. assumed primary responsibility for experimental execution, analysis, codebase and data management; M.T. and B.J.B. supervised the project; R.S.G., N.S., T.A., C.J.W., S.T.M., J.R.W., M.T. and B.J.B. wrote the manuscript with input from all of the authors.

Appendix A: Standard magic-state preparation circuits

Here we describe magic-state preparation circuits with no error suppression, that we compare to our error-suppressed scheme described in the main text.

In Fig. 5(a) we show a circuit that prepares an encoded

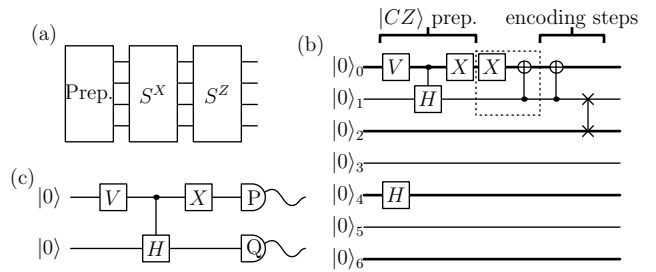


FIG. 5: Magic-state preparation without error suppression. We can encode a physical CZ state using the circuit outlined in (a), where the preparation step, Prep., is shown in (b). The magic state is then encoded using stabilizer measurements S^X and S^Z . The preparation circuit, (b), first prepares a CZ state and two physical qubits before preparing the state to encode it in the four-qubit code by stabilizer measurements. We find that we can simplify the circuit once the CZ state is prepared by making use of its stabilizer operations. As discussed in the main text we observe that the circuit element in the box with a dotted outline acts like a stabilizer on the CZ-state. The inclusion of this stabilizer allows us to remove all of the Pauli-X and controlled-not operations in the circuit, as these circuit elements negate their adjacent self-inverse gates. (c) The CZ state is prepared on two physical qubits. The circuit makes use of $V = \exp(i\theta Y)$ a Pauli-Y rotation with $\tan \theta = \sqrt{2}$, a controlled-Hadamard gate and a bitflip. We perform state tomography on this state by making different choices of single-qubit Pauli measurements, P and Q , on the output of this circuit.

CZ-state by, first, preparing a CZ-state on two physical qubits, then, rearranging the qubits to lie on the data qubits with a swap gate and, finally, measuring the stabilizers of the code to encode the state, assuming we obtain the correct stabilizer measurement outcomes. The circuit used for the preparation step is shown in Fig. 5(b).

We can make use of the stabilizers of the CZ-state to simplify the preparation circuit shown in Fig. 5(b). We define a stabilizer U , with respect to state $|\psi\rangle$, as an operator whose action is trivial on its respective state, i.e., $U|\psi\rangle = |\psi\rangle$. One can check that the CZ state is invariant under the action of a controlled-not gate conditioned on the control qubit in the 0-state

$$CX' = |1\rangle\langle 1| \otimes \mathbb{1} + |0\rangle\langle 0| \otimes X.$$

This unitary gate is equivalent to a standard controlled-not gate, $CX = |0\rangle\langle 0| \otimes \mathbb{1} + |1\rangle\langle 1| \otimes X$, followed by a bit flip on the target qubit, i.e.,

$$CX' = (\mathbb{1} \otimes X)CX.$$

This observation allows us to simplify the preparation circuit. Once the CZ state is prepared, we add the CX' gate in the dashed box in Fig. 5, as the state we have prepared at this stage is invariant under this inclusion. The inclusion of this operator allows us to simplify the circuit, as the repeated application of the two Pauli-X rotations and the two controlled-not operations used in the circuit are in effect an identity operation. We can

therefore omit all of the controlled not operations and the bit-flip operations from the circuit shown. As such, this preparation step only includes two entangling gates: a controlled-Hadamard gate and a swap gate. We perform logical tomography by appending the circuits shown in Figs. 2(b) and (c) to the end of the circuit shown in Fig. 5(a). Likewise, we can perform physical tomography on the output of the circuit shown in Fig. 5(a).

As an aside, we note that the CZ state is also stabilized by the swap gate

$$\text{swap} = (\mathbb{1} + X \otimes X + Y \otimes Y + Z \otimes Z)/2,$$

and CZ as defined in the main text. The CZ state is uniquely stabilized by the Abelian stabilizer group generated by the set $\langle CZ, CX'\text{swap} \rangle$.

Finally, we also compare our error-suppressed magic-state preparation scheme to a circuit that prepares the same magic state on two physical qubits, see Fig. 5(c). We prepare the state on two physical qubits using a single entangling gate, together with single qubit rotations, before measuring the state in varying single-qubit Pauli bases, P and Q , to conduct state tomography on the circuit output.

Appendix B: Device overview

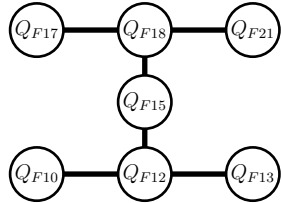


FIG. 6: IBM-Falcon qubit numbering (Q_F)

Encoded state data collection on `ibm_peekskill v2.4.0` spanned several days over a single region outlined in Fig. 6. During this time, monitoring experiments were interleaved with tomography data collection trials. Device coherence times for all qubits exceed $\sim 100\mu\text{s}$ and two qubit error per gate was found to range from 0.35–0.59%. Detailed monitoring of readout errors are provided in Fig. 7(f),(g) and time-averaged readout fidelities ranged from 98.1 – 99.6% for all qubits. Average device characterization data is summarized in Tables I,II. Unencoded magic state data was collected over a single 24-hour period on `ibm_peekskill v2.5.4` on all physical pairs and the best performing edge is reported in Table II. While the unencoded magic state data was not interleaved with encoded state tomography, the best performing pair of physical qubits was found to have a low two qubit error per gate of 0.38% and this error is comparable to the lowest two qubit error per gate for edges used in the encoded magic state experiments.

Appendix C: Real-time feedforward control of qubits

All experiments were performed with IBM Quantum’s first-generation real-time control system architecture. The control system enables collective dynamic circuit control of all qubits with a potential device scaling to hundreds or thousands of qubits. Enabling unified real-time accumulation and processing of mid-circuit measurements and the computation of arbitrary intermediate values through centralized processing. These may then be used as conditions for arbitrarily nested control flow for real-time quantum (circuit) and classical sequences with feedforward gating and measurement operations.

The control system architecture is based on a hierarchical heterogeneous system of FPGA controllers with computing elements for concurrent real-time processing, microwave control, and qubit readout. These are synchronized through a global clock and linked with a real-time communication network to allow synchronized collective operations such as control flow. Branching incurs a constant latency penalty to execute the branch (of order 500ns). Real-time computations will incur a variable latency overhead depending on the complexity of the decision. The system provides specialized fast-path control flow capabilities for rapid and deterministic conditional reset operations. Collective control of the system requires orchestration through a proprietary heterogeneous hardware compiler and code-generator.

These capabilities are programmable through OpenQASM 3, an open-source imperative C-style real-time quantum programming language [33]. All experiments were performed through Qiskit and IBM’s Quantum Services and are available as open-access to device users [34, 35].

Appendix D: State tomography with readout error mitigation using noisy positive operator-valued measurements

The state tomography in the main text uses the qiskit experiments implementation of state tomography [29]. A significant change from previous works is that we do not use readout error mitigation in the main text. Instead we perform tomographic fitting assuming ideal measurements, which attributes any undetectable measurement errors to errors in the reconstructed quantum state. For physical tomography we use the `cvxpy_gaussian_lstsq` fitter with measurement data using the default Pauli-measurement basis on each physical qubit to obtain a weighted maximum likelihood estimate, constrained to the space of positive semi-definite, unit trace density matrices. For logical tomography we use the `cvxpy_linear_lstsq` fitter with a custom measurement basis using Pauli expectation values, rather than Pauli eigenstate probabilities. In this case the custom fitter weights are calculated from the inverse of the stan-

Qubit (Q_F)	Freq. (GHz)	Anharm. (MHz)	T_1 (μ s)	T_2^{echo} (μ s)	EPG (%)	Readout Fid. (%)	$P(0 1)$	$P(1 0)$
10	4.837	-345.0	200.6	120.9	0.027	98.4	0.01612	0.01542
12	4.899	-346.8	289.7	462.6	0.036	98.7	0.01505	0.01068
13	4.972	-345.8	322.4	166.1	0.024	98.1	0.01952	0.01818
15	4.958	-343.8	212.4	200.5	0.036	98.5	0.01658	0.01313
17	5.151	-339.9	256.3	170.7	0.024	99.6	0.00472	0.00305
18	5.083	-341.9	182.2	364.9	0.024	98.7	0.01297	0.01240
21	4.858	-344.2	366.7	362.2	0.012	99.4	0.00318	0.00822

TABLE I: Average single-qubit gate benchmarks on section of ibm.peekskill used in this work.

Gate	CX length (ns)	EPG (%)
12_10	334.2	0.58
15_12	376.9	0.59
13_12	462.2	0.37
15_18	376.9	0.56
18_17	640.0	0.43
18_21	462.2	0.35
18_21*	462.2	0.38

TABLE II: Average two-qubit gate benchmarks on section of ibm.peekskill used in this work. CX gates, constructed from echoed cross-resonance pulse sequence, are specified in one direction, with the reverse directions accessed by addition of single qubit gate. Error per gate (EPG) is extracted from isolated two-qubit randomized benchmarking (spectator qubits idling). The notation * denotes error rates for the best performing physical qubit pair on ibm.peekskill during unencoded magic state preparation experiments defining the minimum (red line) in Fig. 3.

dard error in the Pauli expectation value estimates for each post-selected logical Pauli operator measurement.

Susceptibility to measurement error is a common issue for tomographic methods. In general, tomographic tools are only as good as the noise model of the measurement apparatus, i.e., our ability to calculate the likelihood representing the conditional probability of obtaining a data set given some test density matrix. In this section, we discuss an alternative approach combining readout error characterization with tomographic reconstruction. While the dominant measurement error source in tomography experiments is due to qubit readout, it is a common practice to assume local, uncorrelated readout errors in the Z-basis. A set of noisy positive operator-valued measurements (POVMs) on a single-qubit is,

$$Z'_0 := \begin{bmatrix} 1-p & 0 \\ 0 & q \end{bmatrix}, Z'_1 := \begin{bmatrix} p & 0 \\ 0 & 1-q \end{bmatrix}, \quad (D1)$$

where p (q) is the probability of assigning outcome 1 (0) to a true state $|0\rangle$ ($|1\rangle$); i.e. $p = P(1|0)$ and $q = P(0|1)$. We can also construct noisy POVMs for measurements in the Pauli- X or Pauli- Y eigenbases by rotating the noisy POVMs shown in Eqn. (D1) by an appropriate angle assuming ideal unitaries, since the measurement error is

typically several orders of magnitude greater than the one-qubit gate error.

By interleaving small batches of experimental data collection with readout calibration experiments, one can construct noisy POVMs for each data qubit applicable to a small duration of data collection to be used in fitting procedures discussed above. In Fig. 7 (a), state infidelities from fitting with noisy POVMs can be compared to fitting with ideal projectors ($p, q \equiv 0$), where the latter is reported in the main text. Using readout mitigation the fault-tolerant tomography routines far-outperform both un-encoded tomography, but also the physical tomography of the encoded state. Since the terminating measurements in the logical tomography are very similar to those in the physical tomography, we would expect both of these experiments to demonstrate similar infidelities. Resolving this discrepancy remains an open research question.

It is additionally unclear if our assumed construction of noisy POVMs, or the measured readout error calibrations, collectively reflect the true measurement errors experienced by data qubits. We therefore test the sensitivity of the outcomes of state tomography to the choice of measurement compensation in Fig. 7 (b)-(d). State infidelity is calculated from fitting experimental tomography data to POVMs parameterized by p, q . To simplify, these readout error probabilities are set to be constant for all qubits and time. Dark blue regions of low infidelity (with the minima marked with a red star) do not coincide with the state infidelity calculated using the global average of experimentally measured readout calibrations (marked by a black dot). This disparity suggests that either (a) the target experiments experienced initialization or measurement errors at a higher rate than measured by simpler calibrations and/or (b) fitting with potentially incorrect A -matrices yields a highly non-positive state that is mapped to a high-fidelity physical state under constrained optimization.

Combining readout mitigation with tomography thus remains an open question for further work and results of the main text are limited by unaddressed readout error on terminal measurements. We expect that state tomography experiments in Fig. 7(b)-(e) at $p = q = 0$ provide a reasonable upper bound on the error of the underlying magic state.

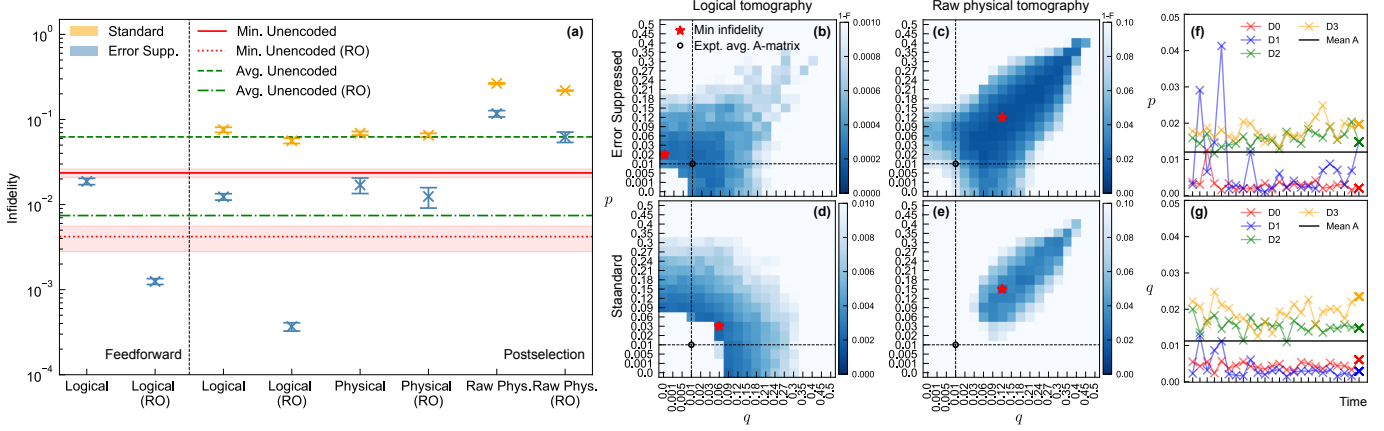


FIG. 7: (a) State infidelity for the standard (orange) vs. error-suppressed (blue) schemes using different tomographic methods; error-bars represent 1σ std. dev. from bootstrapping. On the x -axis, a state is reconstructed with either logical tomography (Logical) or physical tomography after logical projection (Physical); tomography assumes either ideal projectors, as in the main text, or noisy POVMs representing uncorrelated, local readout errors (RO) on terminal data qubit measurements. Raw physical tomography (Raw Phys.) refers to the state on four physical qubits prior to logical projection. Red dotted (green dot-dashed) lines show lowest (average) state infidelities of the two-qubit unencoded magic state prepared with RO mitigation. With RO mitigation, logical tomography outperforms the min. unencoded state supporting conclusions in the main text. (b)-(e) Heatmap of state infidelity vs. avg. measurement error, $p \equiv P(1|0)$, $q \equiv P(0|1)$. Experimental tomography data is fit to noisy POVMs using a parameterized A -matrix, $A := [[1 - p, q], [p, 1 - q]]$, where p, q are constant for all qubits and time. Experimental readout calibrations data are averaged over time and qubits and correspond to a single state infidelity in (b)-(e) (black dots). These state infidelities (black dots) do not coincide with local minima (red stars) or even high-fidelity regions. (f)-(g) Readout calibration measurements of p, q vs. time for all four data qubits over several days; average rates (black solid) are used in (b)-(e) for state fidelities marked by black dots.

Expt. Type	Scheme	Unmitigated		RO Mitigation	
		Mean infid.	σ	Mean infid.	σ
Logical (FF)	Err. Supp.	0.01871	0.00159	0.00125	9.90e-5
Logical (PS)	Err. Supp.	0.01234	0.00106	0.00037	4.10e-5
Physical (PS)	Err. Supp.	0.01699	0.00351	0.01245	0.00336
Raw Phys. (PS)	Err. Supp.	0.11706	0.01008	0.06240	0.00877
Logical (PS)	Standard	0.07570	0.00522	0.05622	0.00401
Physical (PS)	Standard	0.06881	0.00336	0.06529	0.00342
Raw Phys. (PS)	Standard	0.26492	0.00413	0.21861	0.00298
Direct (Min.)	Unencoded	0.02354	0.00271	0.0042	0.0014
Direct (Avg.)	Unencoded	0.06239	0.05620	0.0167	0.0104

TABLE III: Summary of state infidelity results by tomographic experiment, state preparation scheme and readout-error characterization methods with means, standard deviation as shown in Fig. 7.

Appendix E: Analysis in terms of single qubit Pauli errors

The main circuit consists of a set of five syndrome measurements. When measured using the fault-tolerant circuit of Fig. 1, each of these will use two flag qubits. These flag qubits will yield an outcome of 0 unless an error has occurred. Such outcomes are therefore error sensitive events, allowing errors to be detected. Note that for the final S^Z measurement, in the absence of logical tomography, the syndrome result can be inferred from final readout and no flag qubits are used.

Additional error sensitive events come from the results

of the syndrome measurements themselves:

- The results of the two \bar{W} measurements should agree.
- S^X should yield 0, since the system is prepared in a $+1$ eigenstate of this operator;
- Though the first S^Z will yield a random outcome, the following feedforward means that the resulting state is in the $+1$ eigenspace of S^Z . This will then be the expected outcome for the value of final S^Z measurement.

With the six flag results and three expected syndrome

results, there are eleven error sensitive events in all. To analyze the kinds of errors that occur during the circuit, we can first determine the effects of all possible single qubit Paulis inserted into the circuit. Each will be detected by some combination of the error sensitive events, which gives us a signature of this particular type of error.

Note that these signatures are not necessarily unique for each type of error. For example, X and Y Paulis inserted immediately before any measurement will yield the identical effect of a measurement error. We therefore also determine this degeneracy, N_s for each error signature, s .

With this information we can then analyze the syndrome outcomes from experimental data, looking for these signatures and determining the probabilities with which they occur [30]

Due to the limited number of error sensitive events

used in this experiment, these probabilities can be calculated directly. The combined probability, ϵ_s , for all forms of error that lead to a particular signature is determined using the number of shots for which that signature occurs, n_s , and the number of shots for which no error is detected n_0 . The ratio of these numbers of shots will be the ratio of the probability that the error occurs with the probability that it does not,

$$\frac{n_s}{n_0} \approx \frac{\epsilon_s}{1 - \epsilon_s}. \quad (E1)$$

Simply rearranging this relation then gives us the value of ϵ_s . We then use the degeneracy to obtain the average probability for each possible single qubit Pauli error with this signature: ϵ_s/N_s .

[1] R. Harper and S. T. Flammia, Phys. Rev. Lett. **122**, 080504 (2019), URL <https://link.aps.org/doi/10.1103/PhysRevLett.122.080504>.

[2] E. H. Chen, T. J. Yoder, Y. Kim, N. Sundaresan, S. Srinivasan, M. Li, A. D. Córcoles, A. W. Cross, and M. Takita, Phys. Rev. Lett. **128**, 110504 (2022), URL <https://link.aps.org/doi/10.1103/PhysRevLett.128.110504>.

[3] N. Sundaresan, T. J. Yoder, Y. Kim, M. Li, E. H. Chen, G. Harper, T. Thorbeck, A. W. Cross, A. D. Córcoles, and M. Takita, *Matching and maximum likelihood decoding of a multi-round subsystem quantum error correction experiment* (2022), URL <https://arxiv.org/abs/2203.07205>.

[4] L. Egan, D. M. Debroy, C. Noel, A. Risinger, D. Zhu, D. Biswas, M. Newman, M. Li, K. R. Brown, M. Cetina, et al., Nature **598**, 281 (2021), URL <https://doi.org/10.1038/s41586-021-03928-y>.

[5] L. Postler, S. Heuben, I. Pogorelov, M. Rispler, T. Feldker, M. Meth, C. D. Marciniaik, R. Stricker, M. Ringbauer, R. Blatt, et al., Nature **605**, 675 (2022), URL <https://doi.org/10.1038/s41586-022-04721-1>.

[6] R. Acharya, I. Aleiner, R. Allen, T. I. Andersen, M. Ansmann, F. Arute, K. Arya, A. Asfaw, J. Atalaya, R. Babbush, et al., Nature **614**, 676 (2023), URL <https://doi.org/10.1038/s41586-022-05434-1>.

[7] A. G. Fowler, M. Mariantoni, J. M. Martinis, and A. N. Cleland, Phys. Rev. A **86**, 032324 (2012), URL <https://link.aps.org/doi/10.1103/PhysRevA.86.032324>.

[8] D. Litinski, Quantum **3**, 205 (2019), URL <https://doi.org/10.22331%2Fq-2019-12-02-205>.

[9] C. Gidney and M. Ekerå, Quantum **5**, 433 (2021), ISSN 2521-327X, URL <https://doi.org/10.22331/q-2021-04-15-433>.

[10] M. E. Beverland, A. Kubica, and K. M. Svore, PRX Quantum **2**, 020341 (2021), URL <https://link.aps.org/doi/10.1103/PRXQuantum.2.020341>.

[11] F. Thomsen, M. S. Kesselring, S. D. Bartlett, and B. J. Brown, *Low-overhead quantum computing with the color code* (2022), 2201.07806.

[12] L. Z. Cohen, I. H. Kim, S. D. Bartlett, and B. J. Brown, Science Advances **8**, eabn1717 (2022), URL <https://www.science.org/doi/pdf/10.1126/sciadv.abn1717>, URL <https://www.science.org/doi/abs/10.1126/sciadv.abn1717>.

[13] S. Bravyi and A. Kitaev, Phys. Rev. A **71**, 022316 (2005), URL <https://link.aps.org/doi/10.1103/PhysRevA.71.022316>.

[14] A. M. Meier, B. Eastin, and E. Knill, Quantum Info. Comput. **13**, 195–209 (2013), ISSN 1533-7146.

[15] C. Chamberland, K. Noh, P. Arrangoiz-Arriola, E. T. Campbell, C. T. Hann, J. Iverson, H. Puterman, T. C. Bohdanowicz, S. T. Flammia, A. Keller, et al., PRX Quantum **3**, 010329 (2022), URL <https://link.aps.org/doi/10.1103/PRXQuantum.3.010329>.

[16] Y. Li, New Journal of Physics **17**, 023037 (2015), URL <https://dx.doi.org/10.1088/1367-2630/17/2/023037>.

[17] C. Chamberland and A. W. Cross, Quantum **3**, 143 (2019), ISSN 2521-327X, URL <https://doi.org/10.22331/q-2019-05-20-143>.

[18] C. Chamberland and K. Noh, npj Quantum Information **6**, 91 (2020), URL <https://doi.org/10.1038/s41534-020-00319-5>.

[19] S. Singh, A. S. Darmawan, B. J. Brown, and S. Puri, Phys. Rev. A **105**, 052410 (2022), URL <https://link.aps.org/doi/10.1103/PhysRevA.105.052410>.

[20] H. Bombín, M. Pant, S. Roberts, and K. I. Seetharam, *Fault-tolerant post-selection for low overhead magic state preparation* (2022), URL <https://arxiv.org/abs/2212.00813>.

[21] C. Gidney, *Cleaner magic states with hook injection* (2023), URL <https://arxiv.org/abs/2302.12292>.

[22] C. Chamberland, G. Zhu, T. J. Yoder, J. B. Hertzberg, and A. W. Cross, Phys. Rev. X **10**, 011022 (2020), URL <https://link.aps.org/doi/10.1103/PhysRevX.10.011022>.

[23] E. Dennis, Phys. Rev. A **63**, 052314 (2001), URL <https://link.aps.org/doi/10.1103/PhysRevA.63.052314>.

[24] X. Ni, O. Buerschaper, and M. Van den Nest, Journal of Mathematical Physics **56**, 052201 (2015), <https://doi.org/10.1063/1.4920923>, URL <https://doi.org/10.1063/1.4920923>.

[25] M. A. Webster, B. J. Brown, and S. D. Bartlett, *Quantum* **6**, 815 (2022), ISSN 2521-327X, URL <https://doi.org/10.22331/q-2022-09-22-815>.

[26] R. Chao and B. W. Reichardt, *Phys. Rev. Lett.* **121**, 050502 (2018), URL <https://link.aps.org/doi/10.1103/PhysRevLett.121.050502>.

[27] IBM Quantum (2022), URL <https://quantum-computing.ibm.com>.

[28] A. D. Córcoles, M. Takita, K. Inoue, S. Lekuch, Z. K. Minev, J. M. Chow, and J. M. Gambetta, *Phys. Rev. Lett.* **127**, 100501 (2021), URL <https://link.aps.org/doi/10.1103/PhysRevLett.127.100501>.

[29] N. Kanazawa, D. J. Egger, Y. Ben-Haim, H. Zhang, W. E. Shanks, G. Aleksandrowicz, and C. J. Wood, *Journal of Open Source Software* **8**, 5329 (2023), URL <https://joss.theoj.org/papers/10.21105/joss.05329>.

[30] J. R. Wootton, *Syndrome-derived error rates as a benchmark of quantum hardware* (2022), 2207.00553.

[31] M. Takita, A. W. Cross, A. D. Córcoles, J. M. Chow, and J. M. Gambetta, *Phys. Rev. Lett.* **119**, 180501 (2017), URL <https://link.aps.org/doi/10.1103/PhysRevLett.119.180501>.

[32] C. K. Andersen, A. Remm, S. Lazar, S. Krinner, N. Lacroix, G. J. Norris, M. Gabureac, C. Eichler, and A. Wallraff, *Nature Physics* **16**, 875 (2020), ISSN 1745-2481, number: 8 Publisher: Nature Publishing Group, URL <https://www.nature.com/articles/s41567-020-0920-y>.

[33] A. Cross, A. Javadi-Abhari, T. Alexander, N. De Beau-drap, L. S. Bishop, S. Heidel, C. A. Ryan, P. Sivarajah, J. Smolin, J. M. Gambetta, et al., *ACM Transactions on Quantum Computing* **3** (2022), ISSN 2643-6809, URL <https://doi.org/10.1145/3505636>.

[34] URL <https://zenodo.org/record/7591922>.

[35] URL <https://quantum-computing.ibm.com/lab/docs/iql/manage/systems/cite>.